

Supplementary Information

**Simultaneously enabling dynamic transparency control and
electrical energy storage via electrochromism**

Haizeng Li, and Abdulhakem Y. Elezabi**

Ultrafast Optics and Nanophotonics Laboratory, Department of Electrical and Computer Engineering, University of Alberta, Edmonton, Alberta, T6G 2V4, Canada

**To whom correspondence should be addressed.
Email: haizeng@ualberta.ca (Haizeng Li).*

1. EXPERIMENTAL SECTION

A. Chemicals and materials

All solvents and chemicals were of analytical grade and were put to use without further purification. Zinc sulfate heptahydrate ($\text{ZnSO}_4 \cdot 7\text{H}_2\text{O}$, 99%), Aluminum chloride (AlCl_3 , 99%), Potassium chloride (KCl, 99%) and Zinc foil (Zn, 99.9%) were purchased from Sigma-Aldrich. Potassium hexacyanoferrate (III) ($\text{K}_3[\text{Fe}(\text{CN})_6]$, 99%) and Iron (III) chloride hexahydrate ($\text{FeCl}_3 \cdot 6\text{H}_2\text{O}$, 97%) were purchased from Alfa Aesar.

B. Synthesis of the Prussian blue (PB) electrode

The PB electrode was prepared according to the Neff method on an indium tin oxide (ITO) glass (~ 10 ohm/sq.) using a three-electrode configuration,¹ with a Pt wire and an Ag/AgCl as counter and reference electrodes, respectively. The precursor solution for electrodeposition was prepared as in the previous reports.^{2, 3} In a typical procedure, $\text{K}_3[\text{Fe}(\text{CN})_6]$ (10mM), $\text{FeCl}_3 \cdot 6\text{H}_2\text{O}$ (10 mM), and KCl (50 mM) were dissolved in distilled water under stirring. The galvanostatic electrodeposition was performed using an electrochemical workstation (Zennium CIMPS-1). The constant current density (-0.05 mA/cm², 240 s) was selected after carefully screening several electrodeposition protocols. Longer electrodeposition time will lead to the stripping of the PB film after being dried, while the shorter electrodeposition time cannot attain high optical contrast.

C. Prototype device assembly

The smart window ($10\text{cm} \times 8$ cm) was assembled using two pieces of PB electrode as the cathode, a thin strip of Zn foil ($2\text{cm} \times 4.5$ cm) as the anode, 1M ZnSO_4 -KCl as the electrolyte. First, 2mm thick 3M double-sided tape (serving as a spacer to avoid the short-circuit) was laid on the perimeter of the two PB electrodes. Next, a thin Zn foil was sandwiched between the exposed face of the double-sided tape and the electrolyte was injected into the space with a syringe to form the device ($10\text{cm} \times 8$ cm). In the prototype device, the area of the zinc foil ($2\text{cm} \times 4.5$ cm) exposed to the electrolyte is $1.5\text{cm} \times 4.5$ cm.

D. Electrochemical and electrochromic measurements

All the electrochemical and electrochromic measurements were carried out on a Zahner electrochemical workstation. Only the cyclic voltammetry (CV) testing of the PB electrode in 1M ZnSO_4 , 1M AlCl_3 , and 1M KCl were performed via a three-electrode configuration, with a Pt wire and an Ag/AgCl as counter and reference electrodes, respectively. Other electrochemical tests were all performed via a two-electrode configuration. The proportions of Zn^{2+} and $\text{Al}^{3+}/\text{K}^+$ in the dual-ion electrolytes (1M ZnSO_4 - AlCl_3 and 1M ZnSO_4 -KCl) were fixed to be 1:1. In-situ spectroelectrochemical properties of the PB cathodes were tested in a quartz cell by directing a helium neon laser (632.8 nm) through it onto a photodiode, and collecting the data with a storage oscilloscope. Spectroscopy testing was conducted with an Ocean Optics USB4000 Spectrometer, without subtracting the transmittance loss of ITO glass. For the prototype device performance evaluation, prototype devices ($10\text{cm} \times 8$ cm) with 1M ZnSO_4 -KCl electrolyte were assembled using Zn foil as the anode and two pieces of PB electrodes as the cathode. The in-situ spectroelectrochemical property testing and spectroscopy testing of the prototype device are same with the testing of an individual PB cathode.

E. Materials characterizations

X-ray diffraction (XRD, Bruker XRD D8 Discover) with Cu $K\alpha$ -radiation ($\lambda = 1.5406$ Å), X-ray photoelectron spectroscopy (XPS, Kratos AXIS Ultra) with a monochromatic Al $K\alpha$ X-ray source, and field emission scanning electron microscopy (FESEM, Zeiss SIGMA FESEM, German) were

used to identify the phase, morphology, and composition, respectively. FTIR spectrum was measured using a Nicolet 8700 spectrometer. Alpha-Step (IQ -W1-040) was used to reveal the thickness of electrodeposited PB films ($\sim 300\text{nm}$).

2. SUPPLEMENTARY FIG.S AND TABLES

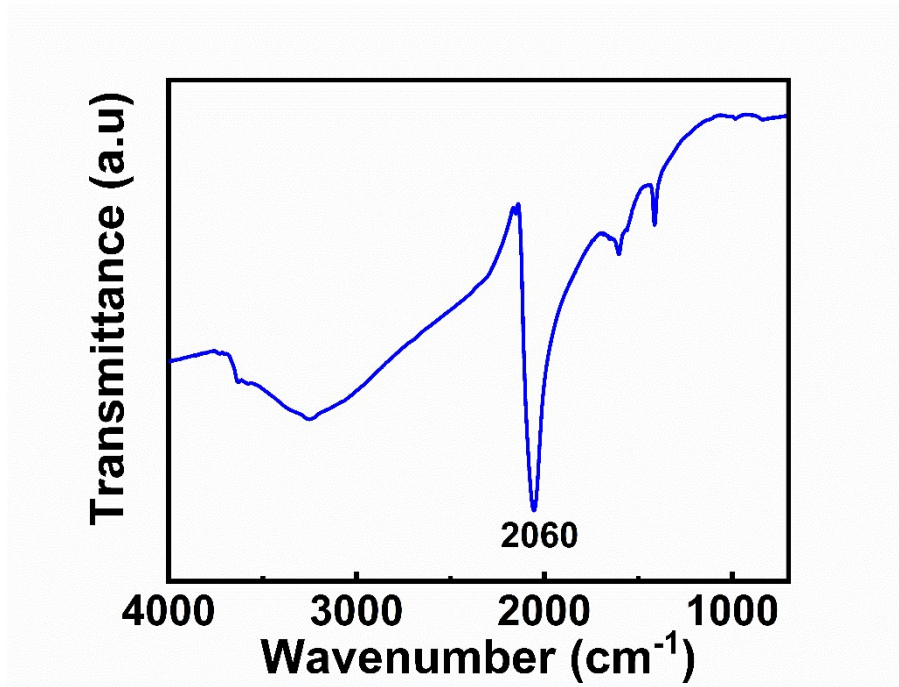


Fig. S1. FTIR spectrum of the electrodeposited PB film.

As shown in Fig. S1, the obvious sharp peak around 2060 cm^{-1} can be assigned to the stretching vibrations of Fe–CN–Fe.⁴ This feature further confirms the successful deposition of the PB film on ITO glass.

Table S1. Redox potentials obtained from the oxidation and reduction peaks of the CV curves shown in Fig. 2c.

Cation	EPC (V)	EPA (V)	EPAR (V)	Radius (Å)
Al ³⁺	0.31, -0.08	0.67, 0.21	0.49	1.9
K ⁺	0.22	0.64	0.43	3.3
Zn ²⁺	0.07, -0.16, -0.38	0.72, 0.52, 0.06	0.40	4.3

EPC and EPA are reduction and oxidation peak potentials, respectively. EPAR is the average redox potential of the most prominent peaks. Radius is the size of the corresponding hydrated cation.

It should be noted that the cations exist in an aqueous electrolyte in the form of hydrated ions. The hydrated ionic radius increases in the order Al³⁺ (1.9 Å) < K⁺ (3.3 Å) < Zn²⁺ (4.3 Å),⁵⁻⁷ and the average redox potential decreases in the same order.

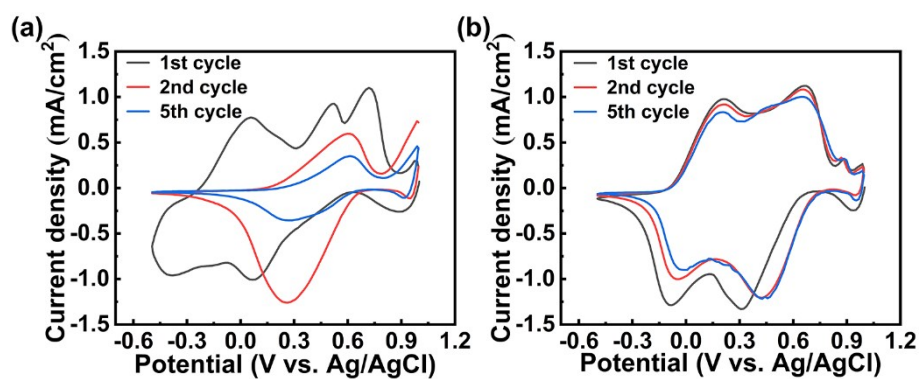


Fig. S2. Cycle-to-cycle CV evolutions of the PB film in (a) 1M ZnSO₄ and (b) 1M AlCl₃, respectively.

Fig. S2(a) shows the redox reaction evolution of the PB film in 1M ZnSO₄ during successive cycling, which is complex compared to that of the PB film in 1M KCl and 1M AlCl₃. The three pairs of redox peaks (0.07/0.72V, -0.16/0.52V, -0.38/0.06V) in the first CV scan are different from the single pair of oxidation and reduction potential peaks observed in the intercalation of K⁺. The two pairs of the redox peaks in lower potentials (-0.16/0.52V, -0.38/0.06V) are assigned to the reduction/oxidation of the high-spin Fe^{II}/Fe^{III} couple binding to the N atoms, while the pair of redox peaks at 0.07/0.72V can be assigned to the reduction/oxidation of the low-spin Fe^{II}/Fe^{III} couple bonding to the C atoms.^{8, 9} Moreover, it is likely that higher electrostatic and steric repulsion originating from the Zn²⁺ intercalation induce the splitting of the reduction/oxidation potential peaks of the high-spin Fe^{II}/Fe^{III} into two pairs.¹⁰ During the subsequent cycles, there are significant changes in the CV curves, which may be attributed to the lattice distortions. The observed one pair of redox peaks at 0.26/0.59 V, assigned to the reduction/oxidation of the low-spin Fe^{II}/Fe^{III} couple bonding to C atom, fades quickly with repeated cycling. This indicates that inefficient and irreversible Zn²⁺ insertion/extraction process is taking place.

As shown in Fig. S2(b), the intercalation of Al³⁺ involves two processes. Overall, the curves are similar to the CV curves of the PB film in 1M ZnSO₄ (Fig. S2(a)). The two pairs of redox peaks (0.31/0.67V, -0.08/0.21V) in the first scan are assigned to the reduction/oxidation of the low-spin Fe^{II}/Fe^{III} and the high-spin Fe^{II}/Fe^{III}, respectively. The positive shift of the peaks during subsequent cycling can be also attributed to the lattice distortions.¹¹

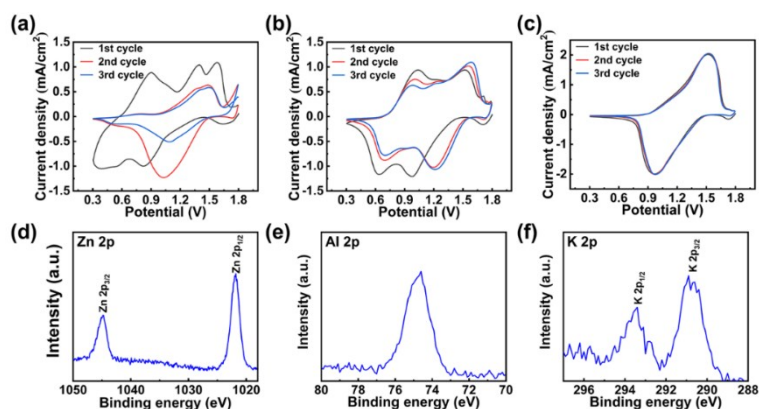


Fig. S3. CV curves of the Zn-PB electrochromic battery in (a) 1M ZnSO₄, (b) 1M ZnSO₄-AlCl₃, and (c) 1M ZnSO₄-KCl, respectively. All the CV tests are conducted via a two-electrode configuration. (d) Zn 2p spectra of self-bleached PB cathode in 1M ZnSO₄. (e) Al 2p spectra of the self-bleached PB cathode in 1M ZnSO₄-AlCl₃. (f) K 2p spectra of the self-bleached PB cathode in 1M ZnSO₄-KCl.

As shown in Fig. S3 (a-c), the CV curves in 1M ZnSO₄, 1M ZnSO₄-AlCl₃, and 1M ZnSO₄-KCl are consistent with the CV curves conducted in 1M ZnSO₄, 1M AlCl₃, and 1M KCl under a 3-electrode configuration (Fig. 2(c,d) and Fig. S2). These results confirm that Zn²⁺ cannot participate in redox reactions in the dual-ion electrolyte systems (1M ZnSO₄-AlCl₃, 1M ZnSO₄-KCl). The XPS results (Fig. S3(d-f)) confirm that the redox reaction mechanism of PB in 1M ZnSO₄, 1M ZnSO₄-AlCl₃, and 1M ZnSO₄-KCl are based on Zn²⁺ intercalation, Al³⁺ intercalation, and K⁺ intercalation, respectively.

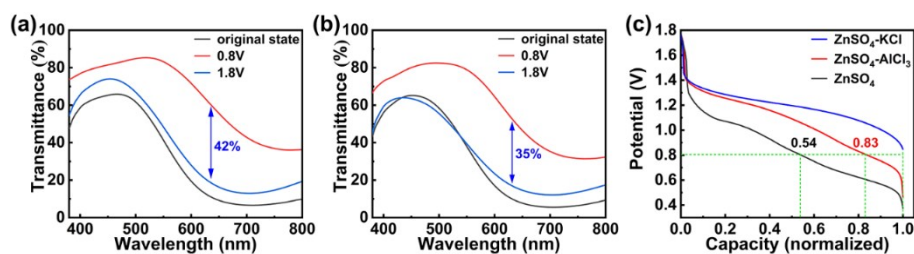


Fig. S4. Visible-near infrared transmittance spectrum of the PB cathode measured under different voltages in (a) 1M ZnSO₄-AlCl₃ and (b) 1M ZnSO₄, respectively. (c) Normalized capacity discharge profiles of the PB cathode in different electrolytes. The capacity normalization was performed by taking the total discharge capacity in the corresponding cycle as unity.

The PB cathode shows the optical contrasts (ΔT) of 42% and 35% at 632.8 nm in 1M ZnSO₄-AlCl₃ and 1M ZnSO₄, respectively (Fig. S4(a,b)). The low ΔT is attributed to the low capacity contribution upon 0.8V. Clearly, the total discharge capacity would result in a fully bleached state; however, only 83% and 54% of the total discharge capacity are achieved upon 0.8V in 1M ZnSO₄-AlCl₃ and 1M ZnSO₄, respectively (Fig. S4(c)). As such, the PB cathode in 1M ZnSO₄-AlCl₃ and 1M ZnSO₄ cannot be fully bleached. Even though the PB cathode can be fully bleached in lower potentials when utilizing 1M ZnSO₄-AlCl₃ and 1M ZnSO₄ as the electrolyte, the low potentials will lead to the low energy retrieval compared to the high discharge potentials.

Table S2. Comparison of electrochromic performance: optical contrast (ΔT) at a wavelength (λ) and switching times (t_c/t_b) of state-of-the-art electrochromic batteries.

Materials	ΔT (%)	λ (nm)	t_c (s)	t_b (s)	Ref.
PB	52.2	670	4.6	4.1(self)	2
$W_{18}O_{49}$	50	650	-	-	12
Mo/Ti:WO ₃	76	632.8	14	-	13
Polypyrrole	59	670	-	6.5 (self)	14
PB	83	632.8	3	8.4 (actual)	This work

self: self-bleaching time

actual: actual-bleaching time

To date, very few reports have fully investigated the electrochromic performance of electrochromic batteries. The 83% ΔT is the highest value to date. The bleaching time of the Zn-PB electrochromic battery system in this work is slightly slower than Refs. 2 and 14. This is because the bleaching time shown in these references are self-bleaching times (the self-bleaching time of Zn-PB electrochromic battery system is measured to be 2.8 s). Compared with the previously reported electrochromic batteries, the Zn-PB electrochromic battery system, utilizing 1M ZnSO₄-KCl as the electrolyte, is considered to be the most promising candidate for electrochromic smart windows.

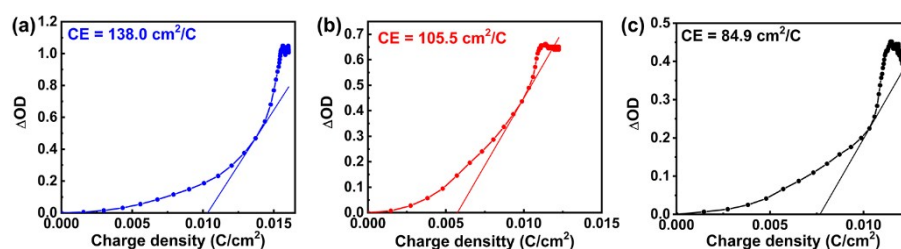


Fig. S5. Coloration efficiencies of the Zn-PB electrochromic battery system in (a) 1M ZnSO₄-KCl, (b) 1M ZnSO₄-AlCl₃, and (c) 1M ZnSO₄, respectively.

As shown in Fig. S5(a), the coloration efficiency of the PB cathode in 1M ZnSO₄-KCl is 138 cm^2/C , which is higher than the values tested in 1M ZnSO₄-AlCl₃ (105 cm^2/C , Fig. S5(b)) and 1M ZnSO₄ (84.9 cm^2/C , Fig. S5(c)). The value of 138 cm^2/C is also higher than the values reported in previous reports.¹⁵⁻¹⁷ This high value indicates that the Zn²⁺/K⁺ dual-ion Zn-PB electrochromic battery system can obtain a large optical modulation with a small energy consumption.

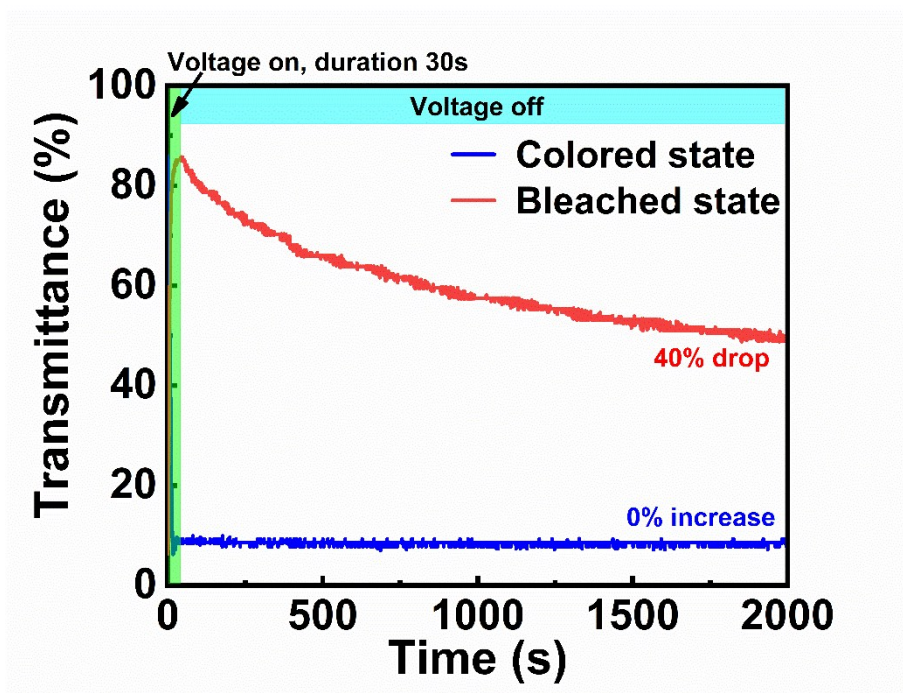


Fig. S6. Transmittance changes monitored at 632.8 nm during open circuit condition after operation at 1.8, and 0.8 V for 30 s, respectively.

Fig. S6 shows the transmittance changes of the $\text{Zn}^{2+}/\text{K}^+$ dual-ion Zn-PB electrochromic battery system over 2000 seconds under the open circuit condition (off-voltage). As shown in Fig. S6, the colored state optical transmittance shows no change under the off-voltage condition, indicating an excellent memory effect in the colored state. The bleached state optical transmittance shows a 40% drop after 2000 seconds, which reveals a self-recharging process. The self-rechargeability, attributed to a spontaneous oxidation process, is similar to previous reports.^{2, 18}

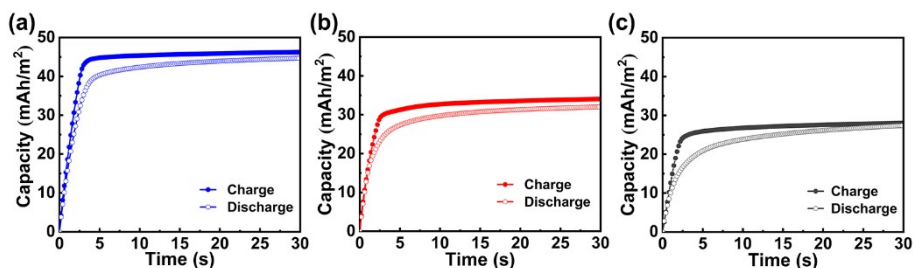


Fig. S7. Charge capacities and discharge capacities during coloration process (1.8 V) and bleaching process (0.8 V) in (a) 1M $\text{ZnSO}_4\text{-KCl}$, (b) 1M $\text{ZnSO}_4\text{-AlCl}_3$, and (c) 1M ZnSO_4 , respectively.

As shown in Fig. S7(a), the charge/discharge capacities of the PB cathode in 1M $\text{ZnSO}_4\text{-KCl}$ are all $\sim 40 \text{ mAh/m}^2$, which are higher than that tested in 1M $\text{ZnSO}_4\text{-AlCl}_3$ ($\sim 30 \text{ mAh/m}^2$, Fig. S7(b)) and 1M ZnSO_4 ($\sim 25 \text{ mAh/m}^2$, Fig. S7(c)). The results are consistent with Fig. S4(c), which confirm the poor electrochromic performance of the PB cathode in 1M $\text{ZnSO}_4\text{-AlCl}_3$ and 1M ZnSO_4 .

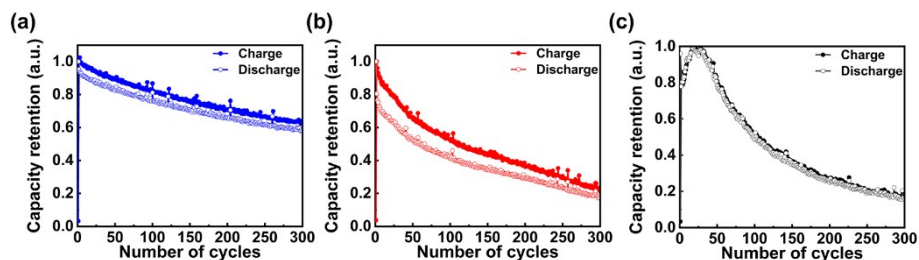


Fig. S8. Cycling stability test of the PB cathode at a current density of 1 mA/cm² in (a) 1M ZnSO₄-KCl, (b) 1M ZnSO₄-AlCl₃, and (c) 1M ZnSO₄, respectively.

As shown in Fig. S8, the PB cathode exhibits ~60% of the initial capacities (including charge capacity and discharge capacity) in 1M ZnSO₄-KCl after 300 cycles, which is much better than the stabilities of the PB cathode in 1M ZnSO₄-AlCl₃ and 1M ZnSO₄ (~20% capacity retention after 300 cycles). Notably, the stability of the PB cathode can be further enhanced via the fabrication of low-defect PB films.¹⁹

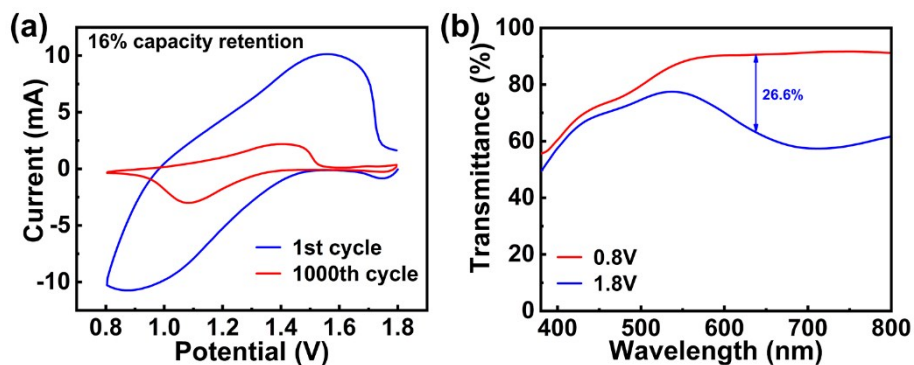


Fig. S9. (a) CV curves of the Zn²⁺/K⁺ dual-ion Zn-PB electrochromic battery before and after cycling 1000 times. (b) Visible-near infrared transmittance spectra for the Zn²⁺/K⁺ dual-ion Zn-PB electrochromic battery after 1000 cycles measured at 0.8 V and 1.8 V.

It is well-known that the response times increase with cycling.²⁰ As such, the most common method for the cycling stability measurement of an electrochromic device, without the influence of the response-times-extension, is to examine the charge capacity retention and optical contrast retention after cyclic voltammetry cycling.²¹ The stability measurements for extended cycles were conducted via the cyclic voltammetric scanning between 1.8V and 0.8V at a scan rate of 100 mV/s. As shown in Fig. S9, the Zn²⁺/K⁺ dual-ion Zn-PB electrochromic battery retains 16% of its initial capacity and has 26.6% optical contrast after 1000 CV cycles. This degradation is attributed to the presence of [Fe(CN)₆] vacancies, as these vacancies can induce lattice distortion during cycling.²² In this regard, the development of PB crystals having low defects would improve the stability of the Zn²⁺/K⁺ dual-ion Zn-PB electrochromic battery.²³

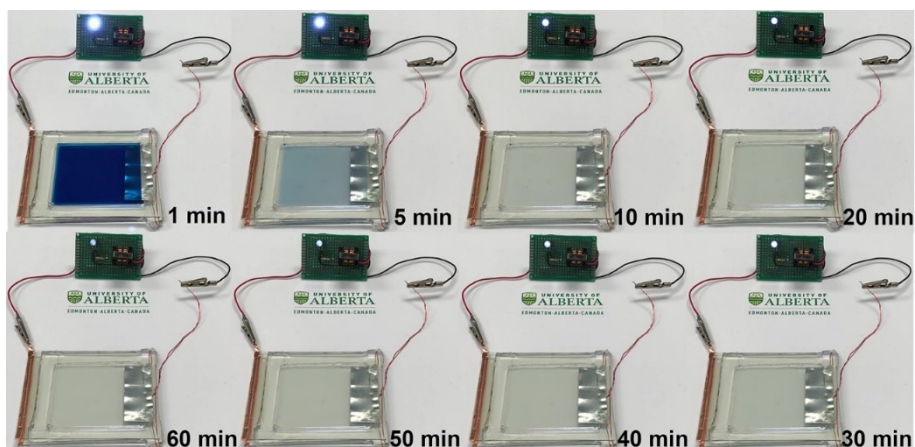


Fig. S10. The self-bleaching process of the prototype device via powering a 0.5 V LED.

As shown in Fig. S10, the prototype device becomes transparent after 10 minutes of powering an LED. Notably, even when the device is bleached, it still powers the LED for more than 60 minutes. This indicates an excellent energy retrieval function of our novel $\text{Zn}^{2+}/\text{K}^{+}$ dual-ion Zn-PB electrochromic battery smart windows.



Fig. S11. The OCV of the prototype device increased to 1.77 V after colored/charged by a 1.8 V external voltage.

3. SUPPLEMENTARY REFERENCES

1. V. D. Neff, *J. Electrochem. Soc.*, 1978, **125**, 886-887.
2. J. Wang, L. Zhang, L. Yu, Z. Jiao, H. Xie, X. W. Lou and X. W. Sun, *Nat. Commun.*, 2014, **5**, 4921.
3. Z. Wang, Q. Z. Zhang, S. Cong, Z. G. Chen, J. X. Zhao, M. Yang, Z. H. Zheng, S. Zeng, X. W. Yang, F. X. Geng and Z. G. Zhao, *Adv. Optical Mater.*, 2017, **5**, 1700194.
4. V. B. Isfahani, N. Memarian, H. R. Dizaji, A. Arab and M. M. Silva, *Electrochim. Acta*, 2019, **304**, 282-291.

5. Z. Li, K. Xiang, W. T. Xing, W. C. Carter and Y. M. Chiang, *Adv. Energy Mater.*, 2015, **5**, 1401410.
6. W. H. Zuo, W. H. Zhu, D. F. Zhao, Y. F. Sun, Y. Y. Li, J. P. Liu and X. W. Lou, *Energy Environ. Sci.*, 2016, **9**, 2881-2891.
7. F. Ming, H. Liang, Y. Lei, S. Kandambeth, M. Eddaoudi and H. N. Alshareef, *ACS Energy Lett.*, 2018, **3**, 2602-2609.
8. Y. Liu, Y. Qiao, W. Zhang, Z. Li, X. Ji, L. Miao, L. Yuan, X. Hu and Y. Huang, *Nano Energy*, 2015, **12**, 386-393.
9. Y. Lu, L. Wang, J. Cheng and J. B. Goodenough, *Chem. Commun.*, 2012, **48**, 6544-6546.
10. R. Trocoli and F. La Mantia, *ChemSusChem*, 2015, **8**, 481-485.
11. H. Y. Fu, C. F. Liu, C. K. Zhang, W. D. Ma, K. Wang, Z. Y. Li, X. M. Lu and G. H. Cao, *J. Mater. Chem. A*, 2017, **5**, 9604-9610.
12. J. Zhao, Y. Tian, Z. Wang, S. Cong, D. Zhou, Q. Zhang, M. Yang, W. Zhang, F. Geng and Z. Zhao, *Angew. Chem. Int. Ed.*, 2016, **55**, 7161-7165.
13. H. Li, L. McRae, C. J. Firby and A. Y. Elezzabi, *Adv. Mater.*, 2019, **31**, e1807065.
14. B. Yang, D. Y. Ma, E. M. Zheng and J. M. Wang, *Sol. Energy Mater. Sol. Cells*, 2019, **192**, 1-7.
15. X. Liu, A. Zhou, Y. Dou, T. Pan, M. Shao, J. Han and M. Wei, *Nanoscale*, 2015, **7**, 17088-17095.
16. Y. Yue, H. Li, K. Li, J. Wang, H. Wang, Q. Zhang, Y. Li and P. Chen, *J. Phys. Chem. Solids*, 2017, **110**, 284-289.
17. J. H. Qian, D. Y. Ma, Z. P. Xu, D. Li and J. M. Wang, *Sol. Energy Mater. Sol. Cells*, 2018, **177**, 9-14.
18. H. Zhang, Y. Yu, L. Zhang, Y. Zhai and S. Dong, *Chem. Sci.*, 2016, **7**, 6721-6727.
19. X. Y. Wu, Y. Luo, M. Y. Sun, J. F. Qian, Y. L. Cao, X. P. Ai and H. X. Yang, *Nano Energy*, 2015, **13**, 117-123.
20. Y. Y. Tian, W. K. Zhang, S. Cong, Y. C. Zheng, F. X. Geng and Z. G. Zhao, *Adv. Funct. Mater.*, 2015, **25**, 5833-5839.
21. A. Llordes, G. Garcia, J. Gazquez and D. J. Milliron, *Nature*, 2013, **500**, 323-326.
22. K. Hurlbutt, S. Wheeler, I. Capone and M. Pasta, *Joule*, 2018, **2**, 1950-1960.
23. Y. You, X. L. Wu, Y. X. Yin and Y. G. Guo, *Energy Environ. Sci.*, 2014, **7**, 1643-1647.